PCCP

Accepted Manuscript

ROYAL SOCIETY OF CHEMISTRY

www.rsc.org/pccp

Controlled Synthesis, photoluminescence, and quantum cutting mechanism of Eu^{3+} doped $NaYbF_4$ nanotubes

Xiangfu Wang,[1*] Chun-sheng Liu,[1] Tonghui Yu,[1] and Xiaohong Yan[1,2*]
[1]College of Electronic Science and Engineering, Nanjing University of Posts and Telecommunications, Nanjing, 210046, People's Republic of China,
[2]College of Science, Nanjing University of Aeronautics and Astronautics, Nanjing 210046, People's Republic of China
Email: xfwang@njupt.edu.cn (Wang) xhyan@nuaa.edu.cn (Yan)

ABSTRACT

Quantum cutting down-conversion has been the subject of intense research activity due to its wide application in optoelectronic devices. However, the energy transfer mechanism behind this down-conversion process is not fully understood. In this work, monodispersed Eu^{3+} doped $NaYbF_4$ nanotubes were synthesized by a hydrothermal route. Simultaneous phase transition from cubic to hexangular and size modification are controlled by changing Eu^{3+} doping concentration. Excited by 393 nm ultraviolet monochromatic light, Eu^{3+} doped $NaYbF_4$ nanotubes show quantum cutting down-conversion involving visible and broadband near-infrared emissions through an energy migration process $^5D_2$ (Eu^{3+}) → $^2F_{5/2}$ (Yb^{3+}) + $^2F_{5/2}$ (Yb^{3+}). Based on emission spectra of Eu^{3+} ions, an improved method is proposed to calculate Judd–Ofelt intensity parameters and radiative transition probability. A comprehensive seven-level rate-equation model is developed to study the energy transfer mechanism. This work offers a method to calculate Judd–Ofelt parameters of opaque powder phosphors and to evaluate population dynamics of excited states.

I. INTRODUCTION

In recent years, near-infrared quantum cutting down-conversion with the quantum efficiency higher than unity has attracted much attention, due to its promising applications in mercury-free fluorescent tubes, plasma display panels and Si solar cells [1–5]. Since the first demonstration of quantum cutting phenomenon in the deep blue region for lanthanide ions Pr^{3+} doped fluorides in the early 1970s [6,7], the focus of research on quantum cutting systems has shifted to the combinations of two ions, such as Tb^{3+}–Yb^{3+}, Tm^{3+}–Yb^{3+}, Eu^{2+}–Yb^{3+}, and Nd^{3+}–Yb^{3+}, in rare earth ions codoped oxide powder and oxyfluoride glass ceramics, in which one ultraviolet photon is converted to two near-infrared photons (λ~1000 nm) [8–18]. So far, there have been few theoretical studies on the quantum cutting mechanism for the Re^{3+}–Yb^{3+} (Re^{3+} = Tb^{3+}, Tm^{3+}, Eu^{2+}, and Nd^{3+}) ion couple. The underlying energy transfer mechanism of the quantum cutting process is still not quite clear, in particular, the population dynamics of excited states of Re^{3+} and Yb^{3+} ions in the cooperative energy transfer process from Re^{3+} to Yb^{3+}.

To study quantum cutting mechanism, it is necessary to calculate Judd–Ofelt intensity parameters Ω_J (J=2,4,6), radiative transition probability, and non-radiative transition probability, before establishing dynamic balance rate equations. The Judd–Ofelt intensity parameters are very important for investigations of local structure and bonding in the vicinity of rare-earth ions [19,20]. The Judd-Ofelt theory was proposed firstly by Judd and Ofelt [21,22], was based on free-ion, static and single configuration approximations, described theoretically the oscillator strength

and radiative transition probability in the $4f^N$ configura-tion of rare-earth ions by considering the electric-dipole and magnetic-dipole contributions. As reported in literatures, Judd-Ofelt optical parameters were calculated through fitting equations with the least square method, after analyzing the absorption spectrum of activated luminescence center ions. However, the Judd-Ofelt theory was used mainly in the form of transparent glass, and was not suitable to powder samples because of adverse light scattering. As for powder sample, the absorption spectrum was obtained by transforming the diffuse reflectance spectrum without consideration of light scattering. Gross errors in this transforming process will induce the inexact values of Ω_J (J=2,4, 6), because the magnitude order of Ω_J is $10^{-20}cm^2$ [19,23]. Thus, there has been few systematic theoretical study focusing on quantum cutting mechanism in powder samples. A new method is necessary to be explored to calculate Judd–Ofelt intensity parameters Ω_J (J=2,4,6) of opaque powder samples.

In this work, we develop a method to calculate experimental Judd–Ofelt intensity parameters Ω_J (J=2,4,6), radiative transition probability A_{ij}, and non-radiative transition probability W_{ij} of Eu^{3+} doped $NaYbF_4$ nanotubes powder through analyzing emission spectra of resulting nanotubes. In conjunction with a dynamic balance rate-equation model, the population dynamics of excited states of Eu^{3+} and Yb^{3+} ions is simulated for the case of excitation by the nanosecond pulse at 393 nm. To our knowledge, quantum cutting down-conversion has not been reported in Eu^{3+} doped $NaYbF_4$ nanotubes previously. The selection of the Eu^{3+} doped $NaYbF_4$ nanotubes powder as the objects of research is motivated by low phonon energy of $NaYbF_4$ host,

the high solubility between Eu^{3+} ions and $NaYbF_4$ host, and high thermodynamical stabilization. Moreover, the $NaYbF_4$ host offers sufficient Yb^{3+} ions with long excited level lifetime as energy-transfer acceptor ions to emit 970~1050 nm infrared light [24-26].

II. Experimental Procedure

Materials: Deionized water was used throughout. Analytical grade NaOH, NH_4F, oleic acid, ethanol, hydrochloric acid, and 99.99% Ln_2O_3 (Ln = Yb and Eu). All chemicals were used as received without further purification.

Synthesis of Eu^{3+} doped $NaYbF_4$ nanotubes:

Eu^{3+} doped $NaYbF_4$ nanotubes were prepared by a hydrothermal method according to the molar composition of $NaYb_{1-x}Eu_xF_4$ (x= 1%, 2%, 3%, 4%, and 5%). In a typical synthesis of process, rare earth oxides Ln_2O_3 (Ln = Yb and Eu) were dissolved in hydrochloric acid (1mol Ln_2O_3 : 3.5mol Hcl) to prepare 0.2 mol/L $LnCl_3$ solution. An aqueous solution of 3.0 mL 0.2 mol/L $YbCl_3$ and $EuCl_3$ was mixed with ethanol (15 mL), oleic acid (15 mL) and NaOH (0.6 g) under thorough stirring. Then, 2 mL NH_4F (0.3889 g) solution was dropwise added to the mixture. After vigorous stirring at room temperature for about 30 min, the colloidal solution were transferred into a Teflon-lined autoclave, sealed and heated. The final products were collected, washed several times with ethanol, and purified by centrifugation.

Characterizations: Structures of the samples were investigated by X-ray diffraction (XRD) using a X'TRA (Switzerland ARL) equipment provided with Cu tube with K_α radiation at 1.54056 Å in the range of $10°\leq 2\theta \leq 70°$. The size and shape

of the samples were observed by scanning electron microscopy (LEO-1530). The size and shape of the samples were observed by a transmission electron microscope (JEOL JEM-2100). The excitation, emission spectra and the fluorescence decay curves in both visible and NIR regions were recorded by a FLSP920 fluorescence spectrophotometer and Shimidazu R9287 photomultiplier (200-900 nm) along with a liquid nitrogen-cooled InGaAs (800-1700 nm) as the detectors. All measurements were performed at room temperature.

III. RESULTS AND DISCUSSION

3.1 Morphology and structure

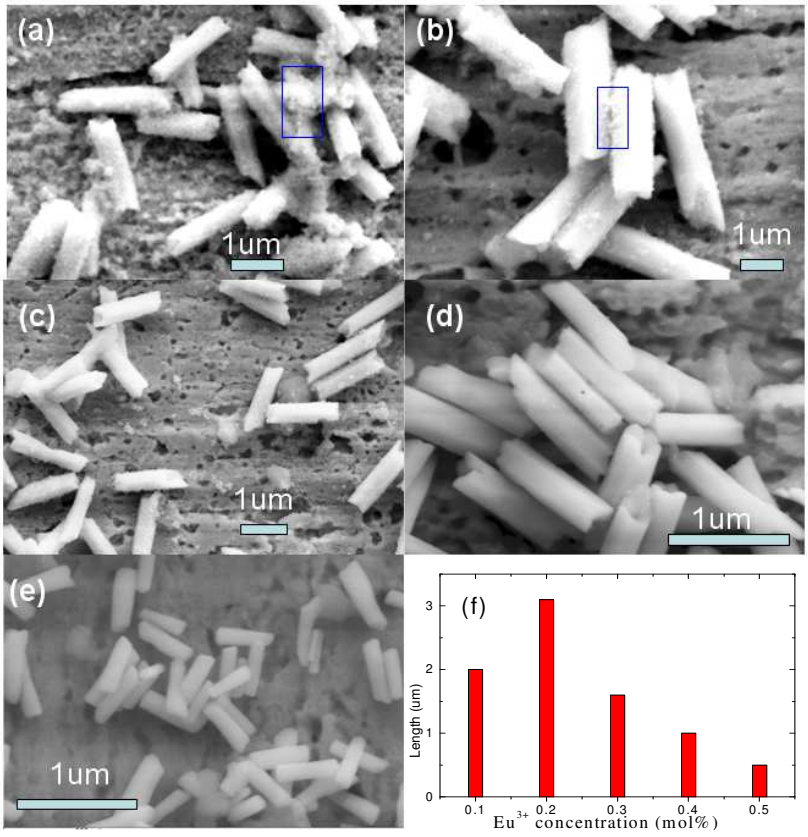

FIG.1. Scanning electron microscopy images of (a) 1%Eu^{3+}, (b) 2%Eu^{3+}, (c) 3%Eu^{3+}, (d) 4%Eu^{3+}, (e) 5%Eu^{3+} doped $NaYbF_4$ nanotubes. (f) Histogram of the average nanotube length.

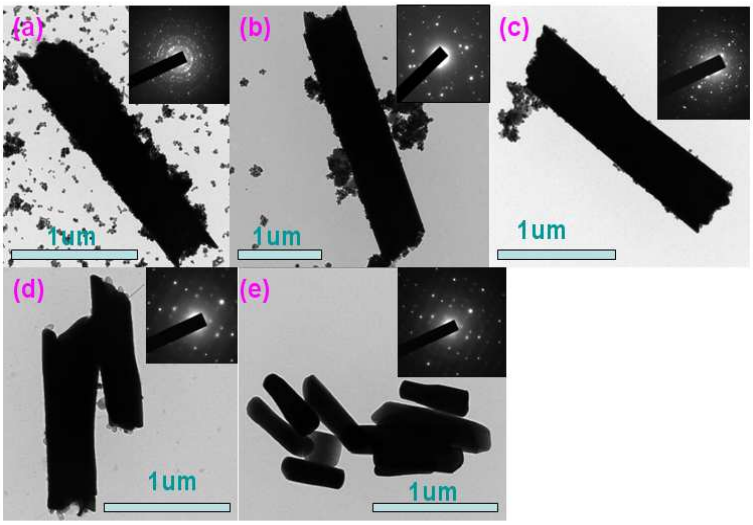

FIG.2. Transmission electron microscope images of (a) 1%Eu^{3+}, (b) 2%Eu^{3+}, (c) 3%Eu^{3+}, (d) 4%Eu^{3+}, (e) 5%Eu^{3+} doped $NaYbF_4$ nanotubes. The insets are corresponding electron diffraction patterns.

Fig.1 shows that the crystal morphology and size of $NaYbF_4$ samples at different Eu^{3+} doping concentrations (1~5mol%) using scanning electron microscopy (SEM). In presence of 1 mol% and 2 mol% Eu^{3+} dopant ions, the scanning electron microscopy images in Fig. 1a and Fig.1b show two distinct particle morphologies that include large nanotubes and small nanoparticles. With increase of Eu^{3+} doping concentration from 3mol% to 5mol%, SEM images show the formation of hexagonal nanotubes (Fig. 1c, 1d and 1e). A phase transition from cubic to hexagonal and size modification from large to small are achieved by increasing Eu^{3+} doping concentration. With increasing Eu^{3+} dopant concentration, nanotubes with different length are formed. The length of nanotubes firstly increases and gradually decreases in the range from 0.5 um to 3.1 um. Transmission electron microscope (TEM) and electron diffraction patterns of the Eu^{3+} doped $NaYbF_4$ samples are shown in Fig.2. The electron diffraction patterns show that polycrystal phase $NaYbF_4$ is transferred into single-crystalline phase $NaYbF_4$ with increasing Eu^{3+} doping concentration.

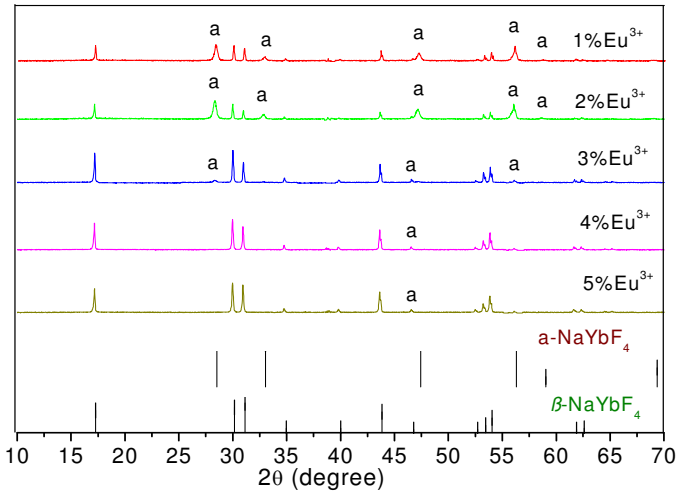

Fig.3. Power XRD patterns of Eu^{3+} doped $NaYbF_4$, and the standard data for α-$NaYbF_4$ (JCPDS 77-2043) and *β*-$NaYbF_4$ (JCPDS 27–1427).

The corresponding X-ray diffraction (XRD) patterns in Fig.3 show the phase conversion process of $NaYbF_4$ crystal from cubic to hexagonal phase with increasing Eu^{3+} doping concentration. Thus, simultaneous phase transition and size modification can be controlled by increasing Eu^{3+} doping concentration. According to reported works [27-29], shape and size modifications were originated from the surface charge redistribution of crystal nucleus induced by inner electron charge transfer between Eu^{3+} doping ions and Yb^{3+} lattice cation ions.

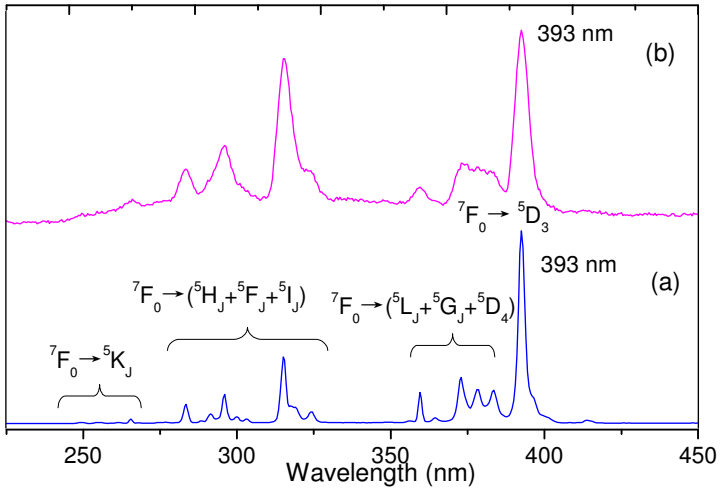

Fig.4. (a) Red 615 nm and (b) infrared 977 nm luminescence excitation spectra of $NaYbF_4$:3%Eu^{3+}.

3.2 Spectrum analysis

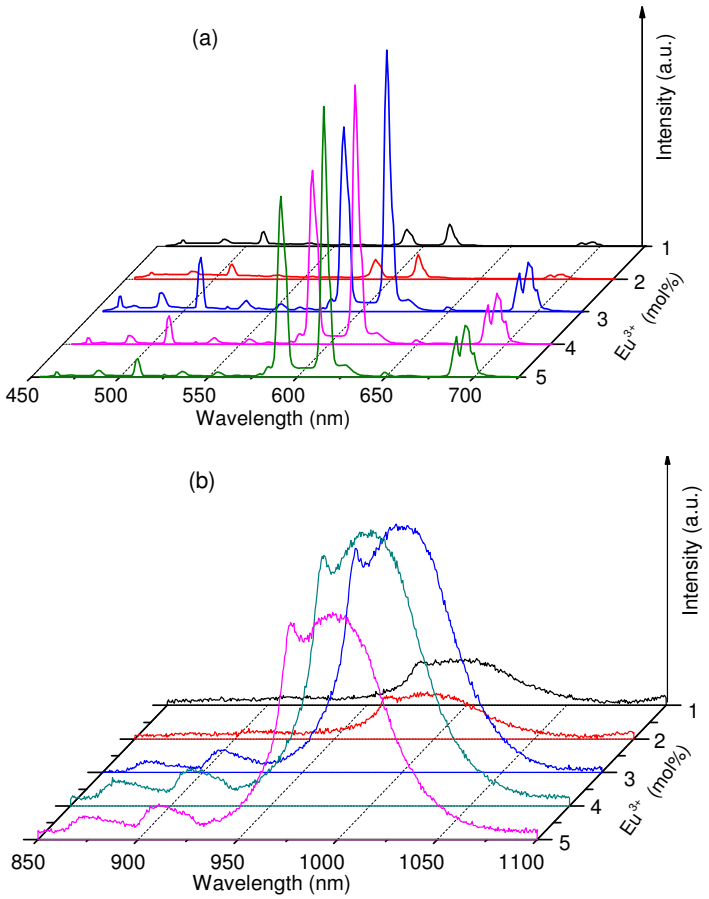

Fig.5. Eu^{3+} concentration dependent emission intensity of (a) visible and (b) infrared luminescence under 393 nm excitation.

Fig.4 shows the excitation spectra of red and infrared luminescence of the $NaYbF_4$:3%Eu^{3+} sample. Fig.4(a) is obtained while monitoring the 615 nm emission line, which corresponds to the $^5D_0 \rightarrow {}^7F_2$ transition of Eu^{3+}. Groups of absorption lines observed in excitation spectrum correspond to $^7F_0 \rightarrow {}^5K_J$, $^7F_0 \rightarrow ({}^5H_J + {}^5F_J + {}^5I_J)$, $^7F_0 \rightarrow ({}^5L_J + {}^5G_J + {}^5D_4)$, and $^7F_0 \rightarrow {}^5D_3$ transitions of Yb^{3+}. Fig.4(b) is obtained while monitoring the 977 nm emission line, which corresponds to the $^2F_{5/2} \rightarrow {}^7F_{7/2}$ transition of Eu^{3+}. One can find that the spectral overlap between the excitation spectra of red 615 nm and infrared 977 nm, is located in the whole wavelength range. The most

intense excitation peak at 393 nm is chosen as excitation source to pump the Eu^{3+} ions.

Fig. 5 shows the room temperature photoluminescence spectra of the Eu^{3+} doped $NaYbF_4$ nanotubes with various dopant concentration with ultraviolet light excitation at 393 nm corresponding to the Eu^{3+}: $^7F_0 \rightarrow ^5L_6$ transition. In the visible region of 450~700 nm, eight emission peaks centered at 465 nm, 488 nm, 510 nm, 555 nm, 591 nm, 615 nm, 650 nm, and 695 nm are observed, which are ascribed to $^5D_3 \rightarrow ^7F_4$, $^5D_2 \rightarrow ^7F_2$, $^5D_2 \rightarrow ^7F_3$, $^5D_1 \rightarrow ^7F_2$, $^5D_0 \rightarrow ^7F_1$, $^5D_0 \rightarrow ^7F_2$, $^5D_0 \rightarrow ^7F_3$, and $^5D_0 \rightarrow ^7F_4$ transitions of Eu^{3+}, respectively. The $^5D_0 \rightarrow ^7F_3$ transition was reported to be originated from an enhanced electron–phonon interaction [30]. In general, the $^5D_0 \rightarrow ^7F_3$ transition is forbidden from both electric (dipole or quadrupole) and magnetic (dipole) considerations. In the infrared region, the broad emission band in the range of 977~1015 nm, which is centered at 997 nm, is attributed to the Yb^{3+}: $^2F_{5/2} \rightarrow ^2F_{7/2}$ transition from the high Stark level of the $^2F_{5/2}$ multiplet to the low Stark level of the $^2F_{7/2}$ multiplet. With the increase of Eu^{3+} concentration from 1 to 5 mol%, the intensity of 465 nm, 488 nm, 510 nm, 555 nm, 595 nm, 615 nm, 650 nm, 695 nm, and 997 nm emission peaks firstly increase and then decrease, a maximum existing at about 3 mol%. An obvious decrease of the intensity of emission bands is observed with increase of Eu^{3+} concentration more than 3 mol%, owing to the concentration quenching [31].

Notably, the energy of the $^5D_2$ level of Eu^{3+} (21355~21396 cm^{-1}) is almost equal to the sum of energy of two excited state Yb^{3+} (10335~10909 cm^{-1}). The cooperative

energy transfer $^5D_2$ (Eu^{3+}) → $^2F_{5/2}$ (Yb^{3+}) + $^2F_{5/2}$ (Yb^{3+}) is possible to occur. In order to explore energy transfer from Eu^{3+} to Yb^{3+}, the Eu^{3+} concentration dependent decay behavior of 488 nm, 510 nm, and 997 nm emissions under 393 nm excitation is studied in Fig. 6. These curves with non-exponential nature reveal the existence of energy transfer from Eu^{3+} to Yb^{3+}. The corresponding decay lifetimes can be calculated by the second order exponential curve fitting:

$$\boldsymbol{I} = A_1\exp(-t/\tau_1) + A_2\exp(-t/\tau_2), \quad (1)$$

where $\boldsymbol{I}$ is the luminescence intensity, A_1 and A_2 are constants, t is the time, τ_1 and τ_2 are the short and long lifetimes for exponential components, respectively. The average

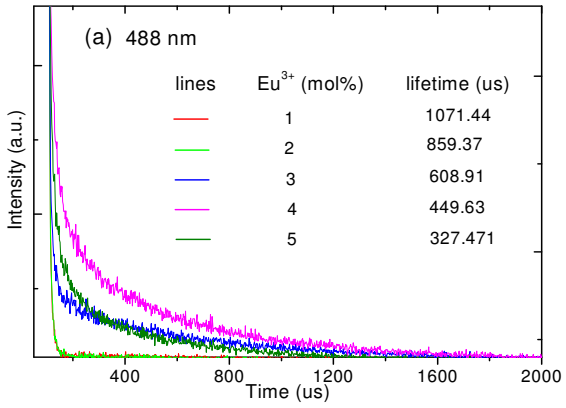

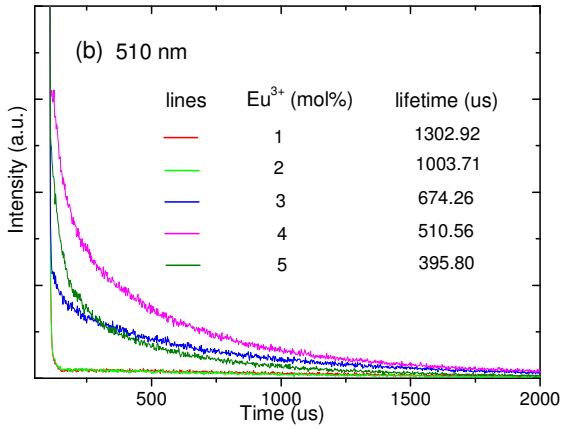

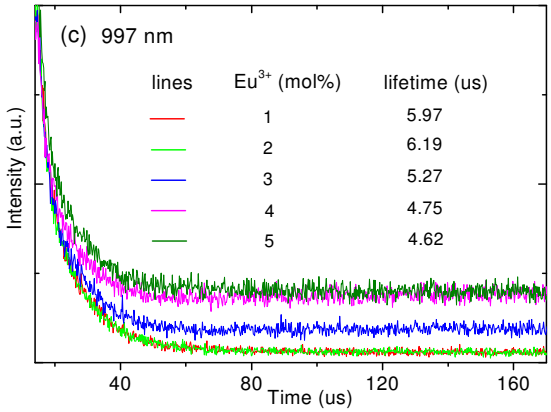

Fig.6. Decay curves corresponding to the (a) 488 nm (b) 510 nm and (c) 997 nm in the Eu^{3+} doped $NaYbF_4$ with different Eu^{3+} concentrations under 393 nm excitation.

decay lifetimes τ are determined by the formula

$$\tau = (A_1\tau_1^2 + A_1\tau_2^2)/(A_1\tau_1 + A_1\tau_2). \quad (2)$$

As shown in Fig.6, obviously, the decay lifetimes of the 488 nm and 510 nm emissions decrease with increase of Eu^{3+} doping concentration. The decay lifetimes of the 997 nm emission firstly increase and decrease with increase of Eu^{3+} doping concentration. These results suggest that the cooperative energy transfer occurs from the $^5D_2$ state of Eu^{3+} to the $^2F_{5/2}$ state of Yb^{3+} under 393 nm excitation.

Based on above analysis, the energy transfer mechanism of infrared quantum cutting from $^5D_2$ (Eu^{3+}) to $^2F_{5/2}$ (Yb^{3+}) under 393 nm excitation is given in Fig.7. The energy of the Eu^{3+}: $^5D_2 \rightarrow {}^7F_0$ transition is two times equal to that of the Yb^{3+}: $^2F_{7/2} \rightarrow {}^2F_{5/2}$ transition, so the excited Eu^{3+} ions can transfer energy to the Yb^{3+} through an energy migration process : $^5D_2$ (Eu^{3+}) → $^2F_{5/2}$ (Yb^{3+}) + $^2F_{5/2}$ (Yb^{3+}). The energy of Eu^{3+} ion on $^5D_2$ level transfer to ground state Yb^{3+} ion, provoking the $^2F_{7/2} \rightarrow {}^2F_{5/2}$ transition of Yb^{3+}, which is a dominant mechanism to achieve 977~ 1015 nm infrared emission.

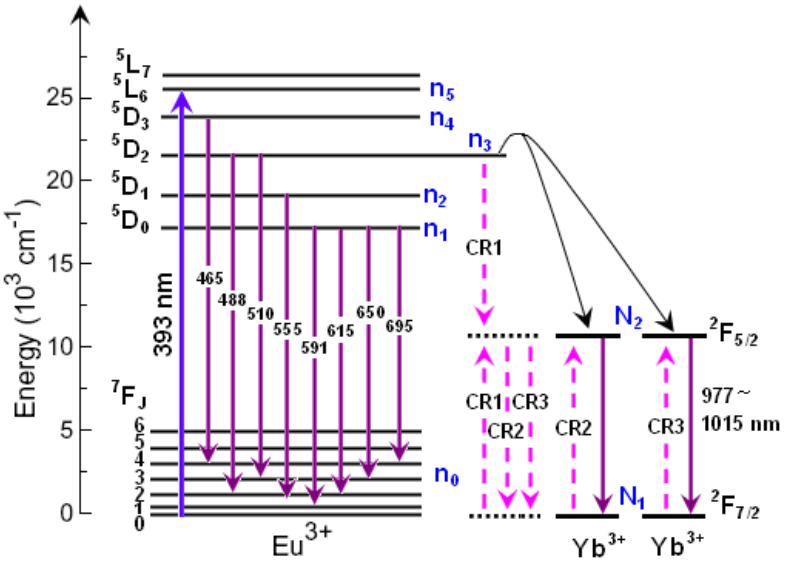

Fig.7. Schematic energy level diagram of Eu^{3+} and Yb^{3+}, illustrating the energy transfer mechanism of infrared quantum cutting from $^5D_2$ (Eu^{3+}) to $^2F_{5/2}$ (Yb^{3+}) under 393 nm excitation. The solid arrows denoted the excitation and the emission processes. The dashed arrows represent cross relaxation energy-transfer processes.

3.3 Rate-equation model for near-infrared quantum cutting

To get some insight into the mechanism of infrared quantum cutting from Eu^{3+} to Yb^{3+}, the Judd–Ofelt theory will be applied for determination of spontaneous emission probability. In this section, we offer a method to calculate experimental Ω_2, Ω_4, Ω_6, radiative transition probability A_{ij}, and non-radiative transition probability W_{ij} of Eu^{3+} doped $NaYbF_4$ nanotubes through analyzing emission spectrum of Eu^{3+} doped $NaYbF_4$ nanotubes. The experimental intensity parameters, such as Ω_2, Ω_4 and Ω_6, are used to calculate spontaneous emission probability A_{ij}.

The luminescence intensity of one emission band can be expressed as

$$I_{ij} = E A_{ij} N_i \qquad (3)$$

where the E is transition energy per photon from $\boldsymbol{i}$ state to $\boldsymbol{j}$ state, A_{ij} is spontaneous radiative emission probability, N_i is the state population of $\boldsymbol{i}$ state [32].

The E is expressed as

$$E = \frac{hc}{\lambda} \tag{4}$$

where λ is the mean wavelength of the transition, *h* the Planck's constant, *c* the speed of light.

For Eu^{3+} ions, the 591 nm emission is originated from $^5D_0 \rightarrow {}^7F_1$ magnetic-dipole transition [33]. The 615 nm and 695 nm emissions are originated from $^5D_0 \rightarrow {}^7F_2$ and $^5D_0 \rightarrow {}^7F_4$ electric-dipole transitions. Electric-dipole spontaneous emission probability $A_{ed\lambda}$ is expressed as

$$A_{ed\lambda} = \frac{64\pi^4 e^2}{3h\lambda^3(2i+1)} \frac{n(n^2+2)}{9} \sum_{t=2,4,6} \Omega_t \left| U^t \right|^2, \tag{5}$$

where e is the elementary charge, *n* the refractive index, $\left| U^t \right|$ the double-reduced matrix element of unit tensor operators, which are considered to be independent of the host and its value has been given by Carnalletal [34]. Magnetic-dipole spontaneous emission probability $A_{md\lambda}$ is expressed as

$$A_{md\lambda} = \frac{64\pi^4 n^3 S_{md}}{3h\lambda^3(2i+1)} \tag{6}$$

Where S_{md} is the magnetic-dipole line strengths. The S_{md} for Eu^{3+} ions is a constant and independent of the medium hosts.

The spontaneous radiative emission probability A_{ij} for electric- and magnetic-dipole transitions is given by:

$$A_{ij} = A_{ed\lambda} + A_{md\lambda} \quad , \tag{7}$$

and the radiative lifetime of an excited state is calculated by

$$\tau_{rad} = 1/A_{ij} \quad . \tag{8}$$

The measured experimental lifetimes (τ_{exp}), the radiative lifetimes (τ_{rad}) calculated

using Eq.(8), and energy transfer probability W_{ET} can be related as follows [19,21]:

$$\frac{1}{\tau_{\exp}} = \frac{1}{\tau_{rad}} + W_{ET}. \quad (9)$$

Notably, the electric-dipole transition $^5D_0 \rightarrow {}^7F_2$ and magnetic-dipole transition $^5D_0 \rightarrow {}^7F_4$ of Eu^{3+} ions are originated from the same $^5D_0$ state of Eu^{3+}. Thus, combing equations (3)~(6), the luminescence intensity of emission bands induced by the magnetic-dipole transition (λ_{md}) and electric-dipole transition (λ_{ed}) are expressed as

$$I_{ed} = \frac{hc\, A_{ed\lambda}}{\lambda_{ed}} N_i, \quad (10)$$

$$I_{md} = \frac{hc\, A_{md\lambda}}{\lambda_{md}} N_i, \quad (11)$$

where N_i is the state population of $^5D_0$ state of Eu^{3+}. Combining above equations, the luminescence intensity ratio of emission bands induced by the magnetic-dipole transition and electric-dipole transition is expressed as

$$R = \frac{\left(n^2+2\right)^2 e^2 \lambda_{md}^4}{9 n^2 S_{md} \lambda_{ed}^4} \Omega_t \left|U^t\right|^2. \quad (12)$$

The luminescence intensity of emission band can be expressed as the integral transition intensity in emission spectrum [35]. Thus, the luminescence intensity ratio R is also expressed as

$$R = \frac{\int I_{ed} d\lambda}{\int I_{md} d\lambda}. \quad (13)$$

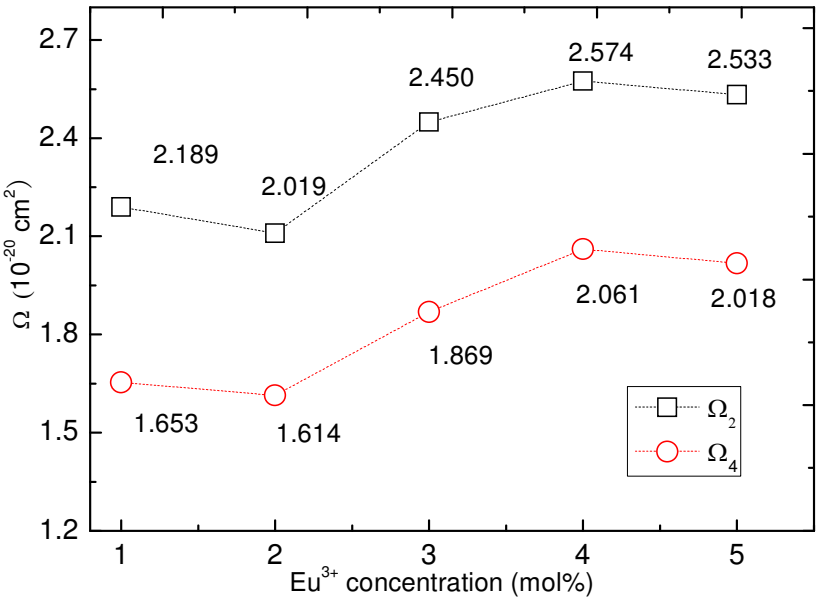

Fig.8. Eu^{3+} concentration dependent Ω_2 and Ω_4 paramaters under 393 nm excitation.

Combining equations (12) with (13), the Ω_2, Ω_4 and Ω_6 can be calculated using a least-squares fitting approach. The Eu^{3+} concentration dependent Ω_2 and Ω_4 paramaters under 393 nm excitation are shown in Fig.8. The Ω_6 is zero, because the $^5D_0 \rightarrow {}^7F_6$ transition is not observed in the emission spectrum of Eu^{3+} doped $NaYbF_4$ nanotubes in Fig.5. Generally, the intensity parameter Ω_2 has been identified to be associated with the asymmetry around the rare earth ions sites and the covalence between the rare earth ions and surrounding ligands, and Ω_4 and Ω_6 are related to the bulk property and the rigidity of host [36]. The Ω_2 changes with increase of the Eu^{3+} concentration, which suggests that the asymmetrical environment around the Eu^{3+} sites is dependent on Eu^{3+} concentration. The Ω_2 reaches a maximum value at 4 mol% Eu^{3+} concentration, which suggests that the weakest asymmetrical environment around the Eu^{3+} sites appears in 4 mol% Eu^{3+} doped $NaYbF_4$ nanotubes. The most intense 997 nm infrared emission in 4 mol% Eu^{3+} doped $NaYbF_4$ nanotubes, shown in Fig.5, is induced by the weakest asymmetrical environment around the Eu^{3+} sites.

In order to study the mechanism of infrared quantum cutting, we study theoretically and experimentally the population dynamics of Eu^{3+} and Yb^{3+} states under the excitation of $^5L_6$ Eu state by the 393 nm ultraviolet monochromatic light. Calculated time dependence of excited state population dynamics is achieved by a simulation of dynamic balance rate equations for Eu^{3+} doped $NaYbF_4$ nanotubes. We assume here the simplest seven-level model in Fig.7:

(1) The ^5D_J (J=0,1,2,3) excited states are populated by the nonradiative relaxation of above $^5L_6$ state. The cross relaxation energy transfer between ^7F_J (J=0,1,2,3,4,5,6) and ^5D_J (J=0,1,2,3) states is negligible.

(2) The adjacent ^7F_J (J=0,1,2,3,4,5,6) states are considered as a ground state.

(3) The infrared quantum cutting process between $^5D_2$ and $^2F_{5/2}$ is equal to three cross relaxation energy transfer processes CR1, CR2, and CR3 to populate the $^2F_{5/2}$ state for two times, due to the energy of $^5D_2$ state is two times equal to that of $^2F_{5/2}$ state.

(4) The energy back transfer from Yb^{3+} to Eu^{3+} is considered to be negligible.

All the processes considered in the system of dynamic balance rate equations are indicated in energy levels scheme in Fig. 7. The population dynamic process of states of Eu^{3+} and Yb^{3+} ions in quantum cutting down-conversion process are simulated as follow:

$$\frac{dn_0}{dt} = A_{10}n_1 + A_{20}n_2 + A_{30}n_3 + A_{40}n_4 - \sigma\rho n_0$$
$$\frac{dn_1}{dt} = W_{21}n_2 - A_{md\lambda}n_1 - A_{10}n_1$$
$$\frac{dn_2}{dt} = W_{32}n_3 - W_{21}n_2 - A_{20}n_2$$
$$\frac{dn_3}{dt} = W_{43}n_4 - W_{32}n_3 - A_{30}n_3 - \delta n_3 N_1^2$$
$$\frac{dn_4}{dt} = W_{54}n_5 - W_{43}n_4 - A_{40}n_4$$
$$\frac{dn_5}{dt} = \sigma\rho n_0 - W_{54}n_5$$
$$\frac{dN_2}{dt} = 2\delta n_3 N_1^2 - 2A_{21}N_2$$
$$n_0 + n_1 + n_2 + n_3 + n_4 + n_5 = 1$$
$$N_1 + N_2 = 1 \qquad (14)$$

where σ is the cross-section of the ground state absorption of Eu^{3+} ions, $\boldsymbol{\rho}$ is the incident pumping power density, $\boldsymbol{n_i}$ is the population number of the $\boldsymbol{i}$th level of Eu^{3+}, $\boldsymbol{N_i}$ is the population density of the $\boldsymbol{i}$th level of Yb^{3+}, the terms of $\boldsymbol{W_{ij}}$ represent the nonradiative decay rates between the levels $\boldsymbol{i}$ and $\boldsymbol{j}$ of Eu^{3+}, $\boldsymbol{A_{ij}}$ is the radiative transition rates between the levels $\boldsymbol{i}$ and $\boldsymbol{j}$ of Eu^{3+} calculated by the Judd–Ofelt parameters from our method, $\boldsymbol{\delta}$ is the probability of energy-transfer from Eu^{3+} to Yb^{3+} involved in the quantum cutting process.

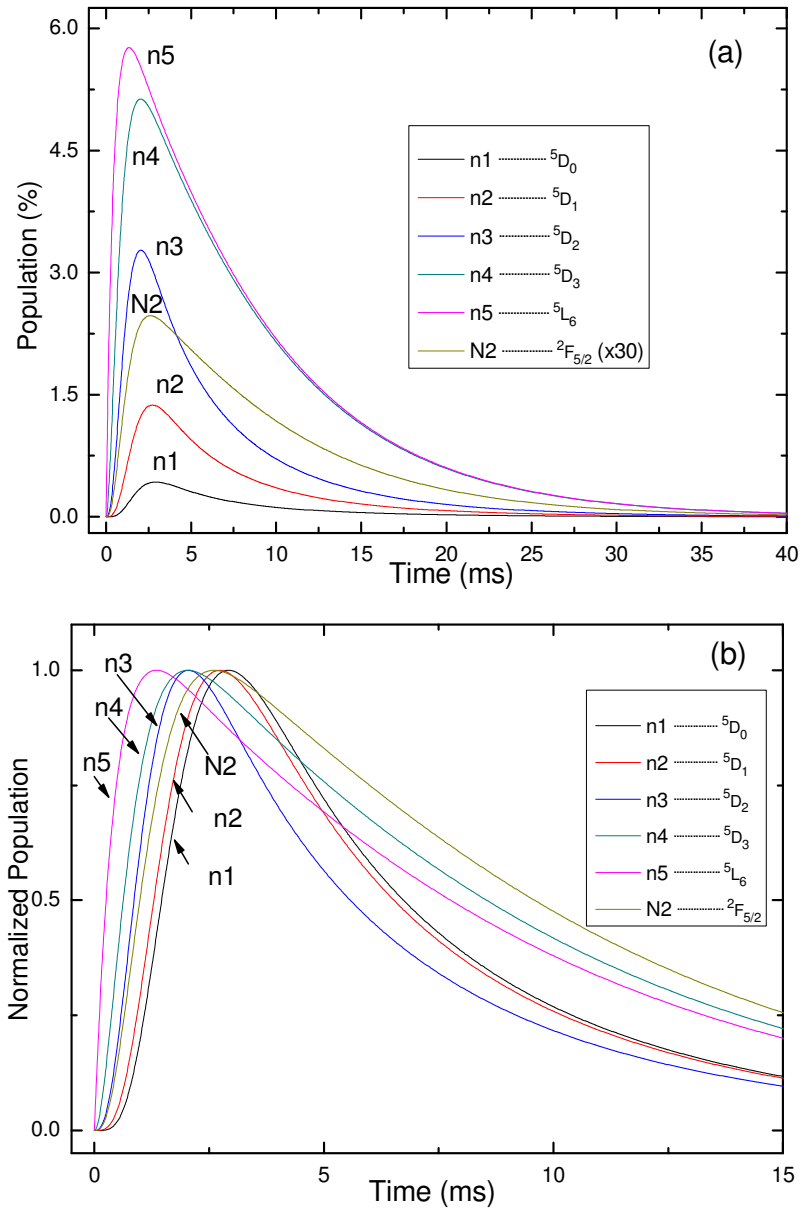

Fig.9. (a) The calculated population of Eu^{3+} and Yb^{3+} excited states: $^5D_0$ (curve n_1), $^5D_1$ (curve n_2), $^5D_2$ (curve n_3), $^5D_3$ (curve n_4), $^5L_6$ (curve n_5) and $^2F_{5/2}$ (curve N_2, the intensity is multiplied by the factor of 30). (b) Normalized population of Eu^{3+} and Yb^{3+} excited states.

For 3 mol% Eu^{3+} doped $NaYbF_4$ nanotubes, the parameter values used in our calculation process are as follow: $A_{10} = 5626.5\ s^{-1}$, $A_{ed} = 46.5417\ s^{-1}$, $A_{20} = 48.7439\ s^{-1}$, $A_{30} = 31.098\ s^{-1}$, $A_{40} = 27.0304\ s^{-1}$, $A_{21} = 113000\ s^{-1}$, $\boldsymbol{\rho} = 7.87\times10^{18}\ mW/cm^2$, $\sigma = 1.92\times10^{-17}\ cm^2$, $\delta = 2287.21\ s^{-1}$, $W_{21} = 1775.84\ s^{-1}$, $W_{32} = 823.8\ s^{-1}$, $W_{43} = 2289.66\ s^{-1}$,

and W_{54} = 2150.54 s^{-1}. The time dependent population numbers of the Eu^{3+} and Yb^{3+} excited states are calculated in Fig. 9(a). The population numbers of $^5D_0$, $^5D_1$, $^5D_2$, $^5D_3$, $^5L_6$, and $^2F_{5/2}$ excited states of Eu^{3+} and Yb^{3+} ions firstly increase sharply and then decrease slowly with time increase. The maximum population numbers of $^5D_0$, $^5D_1$, $^5D_2$, $^5D_3$, $^5L_6$ excited states are about 0.42%, 1.37%, 3.27%, 5.13%, and 5.76% of the total Eu^{3+} number (1.08×10^{19} ions). The maximum population number of $^2F_{5/2}$ excited state is about 0.082% of the total Yb^{3+} number (3.51×10^{20} ions). The normalized population curves in Fig. 9(b) show that different rise times are used to populate Eu^{3+} and Yb^{3+} excited states. The delay time to populate Eu^{3+} excited states gradually increases from $^5L_6$ to $^5D_0$ states, which reveals the below state is populated by the non-radiative relaxation process of above state. The rise time for the population of $^2F_{5/2}$ excited state of Yb^{3+} ions is longer than that for the population of $^5D_2$ state of Eu^{3+} ions reveals the existence of energy transfer from Eu^{3+} to Yb^{3+} in quantum cutting down-conversion process.

IV. SUMMARY

Eu^{3+} doped $NaYbF_4$ nanotubes were synthesized successfully by a hydrothermal route. Phase transition from cubic to hexangular and size modification are achieved by increasing Eu^{3+} doping concentration. Quantum cutting down-conversion from Eu^{3+} to Yb^{3+} ions is observed under 393 nm ultraviolet excitation, in which the energy migration $^5D_2$ (Eu^{3+}) → $^2F_{5/2}$ (Yb^{3+}) + $^2F_{5/2}$ (Yb^{3+}) is the main mechanism to emit near-infrared fluorescence. We proposed a method to calculate the Judd–Ofelt parameters and radiative transition probability of Eu^{3+} doped $NaYbF_4$ nanotubes

through analyzing emission spectra of Eu^{3+} ions. The population numbers of excited states of Eu^{3+} and Yb^{3+} ions are obtained by solving dynamic balance rate equations.

ACKNOWLEDGMENTS

This work was supported by National Natural Science Foundation of China (51032002), the key Project of the National High Technology Research and Development Program (“863” Program) of China (No. 2011AA050526), the Science and Technology Support Plan of Jiangsu Province (BE2011191), Natural Science Youth Foundation of Jiangsu Province (BK20130865), and the Scientific Research Foundation of Nanjing University of Posts and Telecommunications (Grant No. NY213022, and NY213113).

[1] R. T. Wegh, H. Donker, K. D. Oskam, and A. Meijerink, Science **283**, 663 (1999).
[2] P. Vergeer, T. J. H. Vlugt, M. H. F. Kox, M. I. Den Hertog, J. P. J. der Eerden, and A. Meijerink, Phys. Rev. B **71**, 014119 (2005).
[3] F. Lahoz, C. Pérez-Rodríguez, S. E. Hernández, I. R. Martín, V. Lavín, and U. R. Rodríguez-Mendoza, Sol. Energy Mater. Sol. Cells, **95**, 1671 (2011).
[4] J.L.Sommerdijk, A.Bril, and A.W. Jager, J. Lumin. **8**, 341 (1974).
[5] B. S. Richards, Sol. Energy Mater. Sol. Cells **90**, 2329 (2006).
[6] W.W. Piper, and F. S. Ham, J. Lumin. **8**, 344 (1974).
[7] J. L. Sommerdijk, A. Bril, and A. W. de Jager, J. Lumin. **8**, 341 (1974).
[8] S. Ye, B. Zhu, J.X. Chen, J. Luo, and J. R. Qiu, Appl. Phys. Lett. **92**, 141112 (2008).
[9] Q. Y. Zhang, G. F. Yang, and Z. H. Jiang, Appl. Phys. Lett. **91**, 051903 (2007).
[10] X. F. Liu, Y. B. Qiao, G. P. Dong, S. Ye, B. Zhu, G. Lakshminarayana, D. P. Chen, and J. R. Qiu, Opt. Lett. **33**, 2858 (2008).
[11] B. S. Richards, Sol. Energy Mater. Sol. Cells **90**, 1189 (2006).
[12] Z. G. Nie, J. H. Zhang, X. Zhang, and X. G. Ren, Opt. Lett. **32**, 991 (2007).
[13] Q. Y. Zhang, C. H. Yang, and Z. H. Jiang, X. H. Ji, Appl. Phys. Lett. **90**, 061914 (2007).
[14] J.J. Zhou, Y.X. Zhuang, S. Ye, Y. Teng, G. Lin, B. Zhu, J.H. Xie, and J.R. Qiu, Appl. Phys. Lett. **95**, 141101 (2009).
[15] X.F. Liu, Y.B. Qiao, G.P. Dong, S. Ye, B. Zhu, G. Lakshminarayana, D.P. Chen, and J.R. Qiu, Opt. Lett. **33**, 2858 (2008).
[16] D.Q. Chen, Y.L. Yu, H. Lin, P. Huang, Z.F. Shan, and Y.S. Wang, Opt. Lett. **35**, 220 (2010).

[17] D.Q. Chen, Y.S. Wang, Y.L. Yu, P. Huang, and F.Y. Weng, J. Appl. Phys. **104**, 116105 (2008).
[18] Q.Q Duan, F. Qin, Z.G. Zhang, and W.W. Cao, Opt. Lett. **37**, 521 (2012).
[19] U.R. Rodríguez-Mendoza, E.A. Lalla, J.M. Cáceres, F. Rivera-López, S.F. León-Luís, V. Lavín, J. Lumin. **131**, 1239 (2011)
[20] S.H. Huang, S.T. Lai, L.R. Lou, W.Y. Jia, and W.M. Yen, Phys. Rev. B. **24**, 59 (1981)
[21] B.R. Judd, Phys. Rev. **127**, 750 (1962).
[22] G. S. Ofelt, J. Chem. Phys., **37**, 511 (1962).
[23] S.Q. Xu, Z.M. Yang, G.N. Wang, S.X. Dai, J.J. Zhang, L.L. Hu, Z.H. Jiang, J. Alloy. Comp. **377**, 253 (2004).
[24] X.F. Wang, J. Zheng, Y. Xuan, and X.H. Yan, Opt. Express, **21**, 21596 (2013).
[25] M. Wang, C.C. Mi, Y.X. Zhang, J.L. Liu, F. Li, C.B. Mao, S.K. Xu, J. Phys. Chem. C, **113** (44), 19021 (2009).
[26] G.Y. Chen, T.Y. Ohulchanskyy, W.C Law, H. Ågren, and P.N. Prasad, Nanoscale, **3**, 2003 (2011).
[27] F. Wang, Y. Han, C.S. Lim, Y.H. Lu, J. Wang, J. Xu, H.Y. Chen, C. Zhang, M.H. Hong, X.G. Liu, Nature, **463**, 1061 (2011).
[28] X.D. Feng, D.C. Sayle, Z.L. Wang, M.S. Paras, B. Santora, A.C. Sutorik, T.X.T. Sayle, Y. Yang, Y. Ding, X.D. Wang, Y.S. Her, Science, **312**, 1504 (2006).
[29] X.F. Wang, Y.Y. Bu, Y. Xiao, C.X. Kan, D. Lu, and X.H. Yan， J. Mater. Chem. C, **1**, 3158 (2013).
[30] P. Mohanty, and S. Ram, Philos. Mag. Lett., **86**, 375 (2006).
[31] F. Auzel, Chem. Rev. **104**, 139 (2004).
[32] S.G. Xiao, X.L. Yang, Z.W. Liu, and X.H. Yan, J. Appl. Phys., **96**, 1360 (2004).
[33] M. Karbowiak, A. Mech, A. Bednarkiewicz, W. Strek, J. Lumin., **114**, 1 (2005).
[34] W.T.Carnall, P.R.Fields, K.Rajnak, J.Chem.Phys. **49**, 4424 (1968).
[35] W.J. Yang, and T.M. Chen, Appl. Phys. Lett. **90**, 171908, (2007).
[36] A. Balakrishna, D. Rajesh, and Y. C. Ratnakaram, J. Lumin., **132**, 2984 (2012).